Chemical Engineering Journal 166 (2011) 294–305

Contents lists available at ScienceDirect

Chemical Engineering Journal

journal homepage: www.elsevier.com/locate/cej

Investigation of the flow field in a three-dimensional Confined Impinging Jets Reactor by means of microPIV and DNS

Matteo Icardi[a,*], Emmanuela Gavi[a,b], Daniele L. Marchisio[a], Antonello A. Barresi[a], Michael G. Olsen[c], Rodney O. Fox[b], Djamel Lakehal[d]

[a] Dip. Scienza dei Materiali e Ingegneria Chimica, Politecnico di Torino, C.so Duca degli Abruzzi 24, 10129 Torino, Italy
[b] Department of Chemical & Biological Engineering, Iowa State University, 3162B Sweeney Hall, Ames, IA 50011-2230, USA
[c] Dept. of Mechanical Engineering, Iowa State University, 3025 Black Engineering Building, Ames, IA 50011-2230, USA
[d] ASCOMP GmbH, Technoparkstrasse 1, CH-8005 Zurich, Switzerland

ARTICLE INFO

Article history:
Received 19 April 2010
Received in revised form 6 September 2010
Accepted 10 September 2010

Keywords:
Micro-mixer
Confined Impinging Jets Reactor
Micro-Particle Image Velocimetry
Direct Numerical Simulation
Oscillating inflows

ABSTRACT

Micro-mixer devices, such as the Confined Impinging Jets Reactor (CIJR) are currently under study, in particular for precipitation processes of micro- and nano-particles, employed in a variety of applications that include pharmaceuticals, cosmetics, dyes and pesticides. In this work, with the purpose of gaining a better understanding of the main mixing mechanisms occurring in a CIJR, the flow field was studied at four inlet flow rates ranging from $Re = 62$ to $Re = 600$. These conditions correspond to regimes with incipient turbulence in the chamber. Micro-Particle Image Velocimetry (microPIV) experiments and Direct Numerical Simulations (DNS) were performed and compared. MicroPIV is an innovative experimental technique that allows measurement of the instantaneous velocity fields in microfluidic devices. The coupled numerical-experimental approach was found to be essential in understanding and explaining the flow behaviour and the development of turbulence, in particular with respect to the important effects of the inlet boundary conditions. Oscillations present in the inlet flow of the device are in fact primarily responsible for the chaotic and turbulent effects in the reactor. These results provide insights that are important in the development of appropriate computational models for this type of micro-reactor or mixers.

1. Introduction

Ultra-fine or nano-particles turn out to be very useful in a growing number of applications [1,2], in particular in biology and medicine. Many novel processes have been developed in order to produce nano-particles with the desired properties, namely specific particle size distribution, composition and morphology. For example the process of solvent displacement can be employed to produce polymeric nano-particles carrying an active principle to be used in targeted drug delivery [3–5]. In solvent displacement the pharmaceutical active principle and the polymer are dissolved in an organic solvent and then rapidly mixed with an anti-solvent. The faster the overall mixing process occurs, the smaller and the more monodisperse the particles will be. Moreover, efficient mixing dynamics at all scales will foster the interactions between the pharmaceutic active ingredient and the polymer carrier, preventing further particle growth and, in the case of block-co-polymers, tailoring the particle surface with the desired hydrophilic properties.

The necessity of carrying out processes in controlled conditions of rapid mixing, is the main motivation for the development of innovative mixers. A class of mixers designed to operate in turbulent conditions, characterised by dimensions of the order of millimetres, with multiple inlets and a zone of high turbulent kinetic energy dissipation rate, is currently under development. Examples of this kind of mixer configuration are the T-Mixer [6], the Multi-Inlet Vortex Mixer [7,8] and the Confined Impinging Jets Reactor [9,10].

The objective of the present study is to investigate the flow field in a three-dimensional Confined Impinging Jets Reactor (CIJR) with a cylindrical reaction chamber. The CIJR is characterised by two inlets facing each other opening on opposites sides of the reaction chamber. The two inlets are operated at high velocity, therefore they behave as round jets that collide and form an impingement plane where turbulence is developed and the scale of segregation is rapidly reduced. The impingement plane is confined by the mixer head, that at the same time provides a volume in which mixing at the molecular level takes place through diffusion.

Various CIJR geometries and dimensions were studied experimentally by Johnson and Prud'homme [10] and their mixing efficiency was evaluated by means of a parallel competitive reactions scheme. Following that work, Liu and Fox [11] applied

* Corresponding author. Tel.: +39 0115644695; fax: +39 0115644699.
E-mail address: matteo.icardi@polito.it (M. Icardi).

1385-8947/$ – see front matter © 2010 Elsevier B.V. All rights reserved.
doi:10.1016/j.cej.2010.09.046

Computational Fluid Dynamics (CFD) in order to develop a model able to predict the extent of mixing and reaction in the CIJR and found good agreement with the experimental data. They employed the Reynolds-Averaged Navier–Stokes equations (RANS) approach to model the flow field and the Interaction by Exchange with the Mean (IEM) approach coupled with a presumed Probability Density Function (PDF) method (i.e., the Direct Quadrature Method of Moments, [12]) to model micro-mixing. Another work [13] extended the results by considering the effect of the choice of different turbulence models and near wall treatments on the final model predictions, as well as scale up and scale down issues and strategies. The outcome of the latter investigation showed that the choice of the turbulence model and the near wall treatment has a great effect on the final model predictions, and therefore an independent validation of flow and turbulent field is needed.

A useful technique to experimentally investigate the flow field in a CIJR is microscopic Particle Image Velocimetry (microPIV). MicroPIV [14] is a novel experimental technique where instantaneous velocity fields are determined from the displacement of small seed particles. It has been increasingly employed to measure flow fields in planar microfluidic devices (see for example Li et al. [15] and Van Steijn et al. [16]). Recently Liu et al. [17] published data obtained with microPIV for a planar CIJR, the inlet jets of which measure 0.5 mm in width. The experimental flow fields, characterised by a jet Reynolds number between 211 and 1003, were compared with CFD simulation data, obtained with a steady state RANS approach. Though the agreement between experiments and CFD was satisfactory overall, the authors observed that the measured turbulent kinetic energy was larger than CFD predictions, because in the experiments the inlet jets flap significantly at high jet Reynolds number, a phenomenon not predicted by steady state RANS simulations; the authors also suggested that an unsteady model such as Large Eddy Simulation (LES) could be used to improve model predictions.

Many studies exist on free turbulent jets. For example Adrian [18] measured for the first time by means of PIV the instantaneous velocity field of a turbulent circular jet impinging on a plate, thus revealing flow structures and various stages of vortex generation. The same unsteady behaviour for impinging jets that Liu et al. [7] described for the CIJR was observed also in different geometries investigated in other studies. For example Schwertfirm et al. [19] investigated by means of PIV the mean flow and turbulent field in a geometry similar to a T-mixer with round inlets and a square chamber section measuring 80 mm × 80 mm at jet Reynolds number equal to 1270. The experimental measurements were compared to Direct Numerical Simulations (DNS) and, in both experiments and simulations, a flow field symmetry breakage was observed; this demonstrates that it could be a characteristic of the studied mixing device, and not only a product of non-ideal experimental conditions. Santos et al. [20] investigated by means of PIV an axial-symmetric Reaction Injection Molding (RIM) (with inlet jet diameter 1.5 mm and chamber diameter 10 mm) in the jet Reynolds number range from 100 to 500. The study depicted the flow structures characteristic of RIM, in which the jets impingement creates vortexes, with axes perpendicular to the RIM axis.

Various studies in recent years verified the reliability and accuracy of PIV both by comparison versus analytical solutions or DNS and by comparison versus other experimental techniques (e.g. Particle Tracking Velocimetry, Laser Doppler Velocimetry) [21], therefore PIV is now considered a mature tool for investigating the flow and turbulent fields.

Notwithstanding the proven validity of the measurement technique, its application on a small and complex geometry such as that of the CIJR is a novelty and presents many challenges. The CIJR complexity derives from its very small dimensions and from the combined effect that the walls and the impinging jets have on the flow field. Moreover the novelty of the present work is that to our knowledge there is no other published study reporting data obtained with microPIV on a three-dimensional CIJR. As already reported, there are many challenges in the present investigation. Firstly the precise fabrication of such a small device as a micro-mixer is complex and requires specific precision machinery. Secondly, the cylindrical shape of the device and the curved walls of the mixing chamber cause laser light refraction at the interface between the wall and the fluid, a phenomenon that can be alleviated by modifying the fluid refraction index to match the walls material. Thirdly, the control over pumps flow delivery is very difficult to obtain: in particular, it is complicated to obtain equal and perfectly constant flow rates at the two inlets. Finally in microPIV unsteady and highly irregular turbulent flow fields are much more difficult to measure than steady flows. In steady flows accurate data can be obtained by combining the results from many instantaneous images using the sum of correlations technique [22] but in unsteady or turbulent flow, the flow field must be sufficiently seeded so each pair of microPIV images yields an accurate instantaneous velocity field [17].

All these issues are addressed in this work by combining the flow field analysis in a CIJR by means of microPIV with DNS. Nowadays in fact numerical techniques have reached a strong reliability and in particular DNS can be thought as virtual experiments since no approximations are employed when solving the governing continuity and Navier–Stokes equations (under the continuum hypothesis). Of course when working with the DNS the grid has to be fine enough to capture all the length and time scales involved. Therefore DNS can be used also to explain the uncertainty of experimental results underlying effects related to non-ideal experimental setup. This coupled approach reveals to be essential when dealing with the already cited difficulties of microPIV for CIJR investigations.

The manuscript is organised as follows: in the next two sections the experimental and numerical set up, respectively, are presented. The description of the operating conditions investigated in this work follows. The results are finally presented: the flow field is described, focusing on its evolution with the flow regime and fluctuations and spatial correlations are computed and commented. Eventually the main conclusions of the study are summarised.

2. Experimental apparatus and microPIV setup

The geometry of the reactor employed in microPIV experiments is shown in Fig. 1. As can be seen, it is characterised by a cylindrical chamber with a conical head and bottom forming an angle of 45° with the reactor axis. An optically transparent test section was used in the experiments with two inlet pipes that had a diameter $d_j = 1$ mm, a length of 10 diameters and are connected to the pumping system with flexible tubes of the same diameter. The diameters of the chamber and the outlet pipe measure $D = 4.8d_j$ and $\delta = 2d_j$, respectively. The chamber height is equal to $H = 2D$. The coordinate system for the experiments is defined such that the x-axis coincides with the jets axis, while the y-axis coincides with the chamber axis and the origin is centred at the intersection of the two inlet jets.

The experiments were performed for jet Reynolds number ranging from 62 to 600. The jet Reynolds number is defined by the density of the fluid ρ_f, the viscosity of the fluid μ_f, the mean velocity in the inlet pipes u_j, and the inlet pipes diameter d_j as

$$Re = \frac{u_j d_j \rho_f}{\mu_f}. \quad (1)$$

The experimental setup is constituted by the flow delivery facility and by the elements composing the microPIV apparatus, as shown in Fig. 2. The fluid is delivered to the test section by two

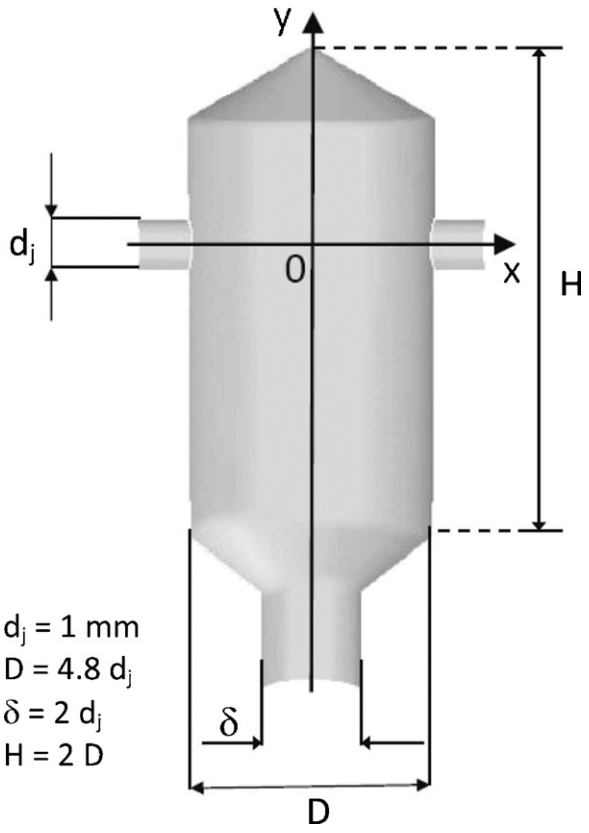

Fig. 1. Sketch of the Confined Impinging Jets Reactor (CIJR) geometry.

micro-gear pumps and pump heads (115 VAC console digital dispensing drive and 0.092 ml/rev suction shoe gear pump head, Cole Parmer Instrument Co., Vernon Hills, IL), each feeding one of the reactor inlets through pipes approximately 50 cm long with the same diameter of the reactor inlets. A reservoir of 150 ml was connected to the flow delivery system with flexible tubing. The plane surface of the test section was placed on the stage of the inverted

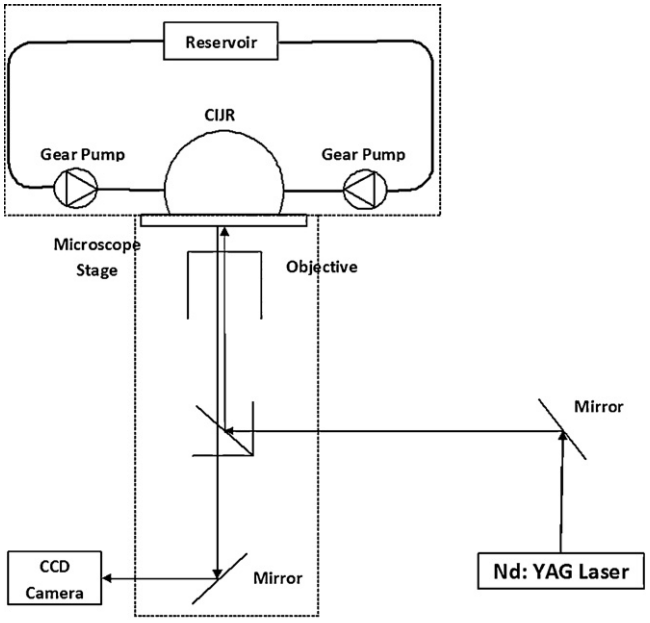

Fig. 2. Experimental set up for microPIV experiments.

biological microscope (Nikon, model T-300 Inverted Microscope). The light beam from the double pulsed laser passes through an optical attenuator to reduce the laser energy per pulse, the maximum energy of which is 120 mJ/pulse, and is then directed to an aperture in the back of the microscope. The laser apparatus (New Wave Research Gemini Nd:YAG PIV laser) emits two independent 532 nm light pulses at a frequency of 4 Hz per pulse pair. Two sequential images are recorded by a CCD camera (LaVision Flowmaster 3 camera, LaVision Inc., Ypsilanti, MI). Images are analysed by the software Davis 6 (LaVision Inc., Ypsilanti, MI) with a cross correlation technique that yields the instantaneous velocity vector field [23].

Since the reactor walls are round, there is a problem of refraction of the laser light at the interface between the fluid and the reactor walls that can be overcome by matching the refractive index of the fluid with that of the Plexiglas (RI = 1.49). The option of using a sodium iodide aqueous solution was discarded because of the resulting high ionic strength, that leads to extensive aggregation of the polymer micro-particles with which the fluid is seeded. An aqueous solution of urea was chosen instead, characterised by a density of $\rho_f = 1.14115\ \mathrm{g/cm^3}$ and a viscosity of $\mu_f = 1.914$ cPs computed by using the equations reported in Kawahara and Tanford [24]. The refractive index of the solution was calculated by extrapolating from experimental data at 20 °C taken at wave-length of 589 nm by applying a linear correlation, that is valid for concentration of urea higher than 2.5 M [25]. An urea solution of 9.38 M resulted in a refractive index of 1.41.

The flow was seeded with fluorescent melamine particles (fluorescent dye rhodamine B: excitation 540 nm; emission 625 nm) characterised by a nominal diameter of 2 μm and density $\rho_p = 1.51\ \mathrm{g/cm^3}$ (G. Kisker GbR, Steinfurt, Germany). These particles have been chosen instead of more common polystyrene micro-particles because of their higher density, lower tendency to aggregation and higher emissivity. By computing the particle Stokes number *St* the ratio of particle response time to the flow time scale can be quantified:

$$St = \frac{\gamma \rho_p d_p^2}{12 \mu_f}, \tag{2}$$

where γ is a characteristic rate of strain for the flow and can be approximated as $\gamma = 2u_j/D$. For the range of *Re* here considered *St* is approximately 3×10^{-4}, therefore it is ensured that particles accurately follow the flow [26].

The seeding concentration was optimised by investigating one of the reactor inlets operating at low flow rate (i.e., $u_j = 0.105$ m/s, $Re = 62$). A range of different seeding concentrations was tested and for each one the root mean square of the velocity was compared to the mean velocity in the inlet, in order to minimise the noise in the measurements. The timing between laser pulses was set such that particles moved approximately one fourth of an interrogation spot between pulses.

Differently from what happens in PIV, where only a thin slice of the flow field is illuminated with a laser sheet, in microPIV the entire volume must be illuminated because of the small length scales involved. There are two consequences related to this configuration. The first one is that the diameter and intensity of a particle image are dependent on the distance from the object plane. The second one is that those particles distant from the object plane form a background glow that makes it difficult to see the near-focus particles [27]. Since particles are flood illuminated in microPIV, rather than illuminated by a laser sheet as in traditional PIV, in microPIV the measurement volume depth (termed *depth of correlation* [27]) depends on primarily the optics of the system [27], but also on Brownian motion [28], on out-of-plane motion [29], and even on fluid shear [30]. In the present experiments the depth of correlation

can be calculated as [27]

$$2Z_{corr} = 2\left[\frac{1-\sqrt{\varepsilon}}{\sqrt{\varepsilon}}\left(f^2 d_p^2 + \frac{5.95(M+1)^2\lambda^2 f^4}{M^2}\right)\right]^{1/2}. \quad (3)$$

In the above equation $\varepsilon = 0.01$, M is the magnification, λ is the wavelength of fluorescence emitted by the particles, f is the focal number of the lens and can be related to the numerical aperture (NA) by the following

$$f = \frac{1}{2\mathrm{NA}}. \quad (4)$$

In the present experiments, a $4\times$ 0.2 NA objective was used with a $0.45\times$ coupler, yielding a depth of correlation of 47 μm.

A multi-pass interrogation scheme with decreasingly smaller window sizes and a 50% overlap between adjacent interrogation spots was used with a final interrogation spot size measuring 16×16 pixels. The post-processing performed on the vector field consisted in the removal of "bad" vectors (i.e. too different from their neighbours average) that are replaced with interpolated values. Readers interested in the details of the "bad" vector removal process are referred to the specialised literature [23]. The final spatial resolution was 140 μm in both the x- and y-directions.

3. Direct Numerical Simulations and numerical details

The flow field in the CIJR is simulated by directly solving the continuity and Navier–Stokes equations for an incompressible fluid in three dimensions:

$$\nabla \cdot \mathbf{U} = 0, \quad (5)$$

$$\frac{\partial \mathbf{U}}{\partial t} + \mathbf{U}\cdot\nabla\mathbf{U} = -\frac{1}{\rho_f}\nabla p + \nu_f \Delta \mathbf{U}, \quad (6)$$

where ν_f is the kinematic fluid viscosity. When DNS is employed the governing equations are solved without any model. Therefore, if the grid is fine enough and the numerical discretisation scheme is accurate enough, the flow is described in detail by resolving all the time and length scales involved in the turbulent flow. In this respect, fully resolved DNS are virtual experiments that can be used to understand and interpret experimental data.

Computations are carried out with the commercial Computational Multi-Fluid Dynamics (CMFD) code *TransAT* [31]. The equations are solved with a finite volume approximation, where the pressure–velocity coupling is performed by using the SIMPLEC algorithm. Time discretisation is performed with a 2nd order implicit scheme or with a 3rd order explicit Runge-Kutta scheme. The advective terms are discretised with both the classical QUICK scheme and the HLPA scheme [32], which combines a second-order upstream-weighted approximation with the first-order upwind differencing under the control of a convection boundedness criterion. Although HLPA is not the most common scheme for DNS, it assures a better convergence and stability, especially in the initial transitory part of the simulations. The simulations were performed also with the QUICK scheme and the CDS and they revealed no significant differences. Solid boundaries of the reactor are represented with the Immersed Surface Technique (IST) in which the cells near the walls are marked using a signed distance function (known as the solid level-set function) and treated in a separate way to impose no-slip condition there. By employing this technique the walls can be immersed in a Cartesian grid, which results in a reduced meshing time and a higher accuracy of the numerical schemes, since the numerical viscosity due to grid-skewness is simply eliminated [33]. These two elements make the IST approach very useful to simulate unsteady turbulent flows with DNS in complex geometries.

Five different grids were prepared to optimise the computing time and ensure that for each investigated case all the scales were resolved. Details about the grids (within the IST context) are reported in Table 1. After a dimensional analysis, explained in the next section, and the comparison of results obtained with different grids for a test case, it was found that grid 2 was able to capture all the relevant length scales for the two lowest flow rates, while for the two highest flow rates a more refined grid must be used. In this case grid 3 was found to be fine enough since the local ratio between the mean cell size and the approximated minimum length scale of the flow is always between 0.5 and 2. The details about the estimation of the minimum length scale of the flow are reported in the next section. Simulations were performed on a Linux cluster (10×8 CPUs AMD Opteron, 2.44 GHz) with either a shared or a distributed memory parallelism. The former was used with single-block grids (Open-MP library) and the latter with multi-block grids (MPI library). Using eight processors with shared memory and a speed-up factor of about 3.5, the total CPU time needed to simulate 1 s of real time with grid 2 was found to be between 1 and 4 days depending on the flow regime which influence the convergence and the simulation time step.

Table 1
Computational grids used for simulations: grid number, number of cells per block, number of blocks, number of internal cells used for computing the flow, cells size and parallelization library.

	Cells per block	Blocks	Internal cells	Δx, μm	Parallel
1	$40\times40\times80$	1	1×10^5	100–140	O-MP
2	$68\times60\times128$	1	3.5×10^5	50–80	O-MP
3	$100\times84\times150$	1	8.5×10^5	30–60	O-MP
4	$46\times42\times34$	36	8×10^5	50–60	MPI
5	$82\times52\times66$	36	8×10^6	17–25	MPI

4. Operating conditions investigated and boundary conditions

The flow field was measured and simulated for four inlet jet Reynolds numbers (Re): 62, 150, 310 and 600, corresponding to actual average inlet velocities (u_j) of 0.105, 0.250, 0.520, 1.01 m/s. For all the four cases the flow in the inlet pipes is laminar, however inside the chamber a transition occurs; the impingement in fact, creates strong instabilities and drive the flow towards turbulence. In Table 2 the operating conditions are summarised reporting for each flow rate the mean inlet velocity, the mean residence time in the CIJR, the inlet jet Reynolds number and the approximated Kolmogorov micro-scale. The estimation of this length scale is a very challenging issue since the flow under study may be not under fully developed turbulence and the statistical theory of turbulence is not guaranteed to be valid here. Nevertheless this is a crucial point to make sure that a DNS simulation is actually resolving all the time- and length-scales involved. As it is well known, for high Reynolds number flows it is possible to estimate the Kolmogorov length as

$$\lambda_K = \left(\frac{\varepsilon}{\nu_f}\right)^{1/4},$$

where ε is the dissipation rate of turbulent kinetic energy. The turbulent kinetic energy can be measured from experiments or

Table 2
Nominal flow rates, mean velocities, mean residence times, jet Reynolds numbers and estimated Kolmogorov micro-scale lengths.

FR, ml/min	Mean inlet velocity, m/s	τ_R, s	Re	λ_K, μm
10	0.105	1.05	62	–
20	0.25	0.44	150	–
40	0.52	0.21	310	–
90	1.01	0.11	600	≥17

calculated by solving an appropriate transport equation, while its dissipation rate can be estimated with a mixing length hypothesis or by solving another transport equation. This is the standard procedure of many RANS models. For the flow under study it is reasonable to apply these concepts, at least for the highest flow rate studied, corresponding to $Re = 600$. In particular, the results of the work of Hosseinalipour and Mujumdar [34] in which different RANS models were compared for impinging opposing jets in a flow regime very similar to this study, show that the Abe–Kondoh–Nagano Low-Reynolds number model [35] is able to describe accurately opposing impinging jets flow. This model, in fact, was found to be the most appropriate for this type of flows and resulted in an estimation of the maximum turbulent energy dissipation rate localised in two zones on the inlet axis, 1 mm far from the centre. With these values an estimated Kolmogorov length of $\lambda_K = 17\ \mu m$ for the case of $Re = 600$ was obtained (after reaching a grid independent solution). As already mentioned, this estimation can be applied only for the highest flow rate but we can suppose that, for lower flow rates, the minimum length scale could not be smaller. Of course the flow condition in the CIJR under study are not "ideal" but this is still a reasonable lower limit approximation. Simulations with other RANS models in fact gives a similar or even higher estimation of this length scale. Based on these additional arguments it is possible to conclude that the grids adopted in this DNS study are adequate.

In the experiments, the objective was focused on the plane passing through the jets and the chamber axes. Before taking images, some time was allowed for the flow to reach a steady state. The inlet flow rate was adjusted from the pumps in order to obtain the balancing of the jets. For each jet Reynolds number 1000 realisations were captured and analysed. The microPIV images formed using the 4× objective and the 0.45× coupling cover an area of approximately 4.6 mm × 3.68 mm, however the measured area does not cover the entire width of the reactor, but is limited to an area 4.0 mm × 2.5 mm due to the cylindrical shape of the device, that causes the shading region near the wall and an uneven illumination that favours the measurement in the central region of the interrogation window. The images are centred at the intersection between the jets and chamber axes.

Experimental results and DNS predictions were compared in the same window captured by microPIV and a numerical filter equivalent to the experimental one was developed to spatially smooth data coming from the simulations, which are finer than microPIV resolution for all the grids. In fact, comparing the microPIV resolution with the size of the computational cells, one finds that simulations are characterised by a better resolution of smallest scales. This does not affect much the comparison of first order statistics (i.e., mean velocities) but can in principle compromise the comparison of second order statistics (i.e., velocity fluctuations). In this case however it was found that the filtering operation simply reduce the mean oscillations of a small percentage (less than 5%) so only the unfiltered results are shown.

Simulations data were saved and analysed for each time step (calculated adaptively according to stability criteria based on Courant–Friedrichs–Lewy and diffusion conditions [33]) after the transient in a time window of length equivalent to three residence times for the two lowest flow rates and six residence times for the highest ones. MicroPIV results instead are recorded with a time step of a quarter of second for a total experimental time of 250 s. It resulted that the time steps used for numerical simulations is often more than a thousand times smaller than the experimental one. Also the total time of analysis is very different. This complicates the comparison between experiments and simulations since only the latter ones can give a complete description of the transient development of the flow. MicroPIV can instead be used to image instantaneous velocity fields and to calculate statistics which are needed for the simulations setup.

Contrary to what happens with RANS, when employing DNS or LES, the results are very sensitive to boundary conditions and the proper selection of inflow boundary conditions becomes crucial. In fact, no time averaging is performed and the system is highly sensitive to the instantaneous jets behaviour. For this reason the microPIV data in the inlets were analysed revealing small variations in time which could not be related to natural instabilities in the system or to turbulence in the chamber. They are instead related to the pumps feeding the solution to the CIJR. Therefore to clarify the effect of the experimental inflows two types of simulations were performed with different boundary conditions.

First a set of simulations were performed with constant laminar inflow profiles:

$$\mathbf{U}(\mathbf{x}) = \begin{pmatrix} U_x|_{inlet} \\ U_y|_{inlet} \\ U_z|_{inlet} \end{pmatrix} = \begin{pmatrix} U_0(\mathbf{x}) \\ 0 \\ 0 \end{pmatrix} \tag{7}$$

where $U_0(\mathbf{x})$ is the constant parabolic profile in the tubes which depends on the wall distance, then the inflows were approximated as follows:

$$\mathbf{U}(\mathbf{x}) = \begin{pmatrix} U_x|_{inlet} \\ U_y|_{inlet} \\ U_z|_{inlet} \end{pmatrix} = \begin{pmatrix} U_0(\mathbf{x})[1 + K\cos(t\omega + \phi)] \\ 0 \\ 0 \end{pmatrix} \tag{8}$$

by superposing to the constant profile a single harmonic with amplitude K (ranging between zero and 0.2), and frequency ω ($\approx 10(u_j/D)$) chosen according to experimental data. To emphasise the effects of these oscillations the phase lag between the two inlets was set to $\pi/2$ in order to result in phase opposition. Since the time interval between the experimental measurements of the inlets is relatively large and of the same order of magnitude of the total simulations time ($\Delta t_{microPIV} = 0.25$ s), an exhaustive analysis of the inflow time series is not possible especially when the flow rate is high and the inflows are more unsteady. For this reason the calculation of the boundary conditions parameters was carried out for the two lowest flow rates, analysing the time spectra, and only estimated for the two highest ones. Due to this lack of data in time and to the strong feedback (for high flow rates) of the internal flow to the velocity measured at the inlet, it was not possible to investigate in more depth the experimental inflows, recovering for example more frequencies or imposing exactly the velocity measured by experiments. However, the assumption of a single frequency can be physically explained by an oscillation due to the mechanical features of the whole pumping system and it was found to be sufficient to catch the observed behaviour.

5. Results and discussion

The cylindrical geometry of the reactor creates a three-dimensional flow field which is reproduced also in the simulations. MicroPIV measurements were obtained the xy-plane with $z = 0$ therefore all the results are analysed in this plane. However the z-component of the flow has a strong influence on the development of turbulence, as it can be seen in the results and which would be completely neglected if a planar reactor or bi-dimensional simulations were considered instead.

The flow field is first discussed qualitatively by analysing snapshots of the instantaneous and the mean flow field measured with microPIV to show the main feature and structures of the flow. MicroPIV asymmetry is then underlined looking at the mean x-velocity (U_x^{MEAN}) along y-direction at the two inlets and in the centre of the reactor. After this overview of the experiments a detailed comparison between microPIV and simulations in terms of first (i.e., mean velocity, U^{MEAN}) and second order statistics (i.e., root-

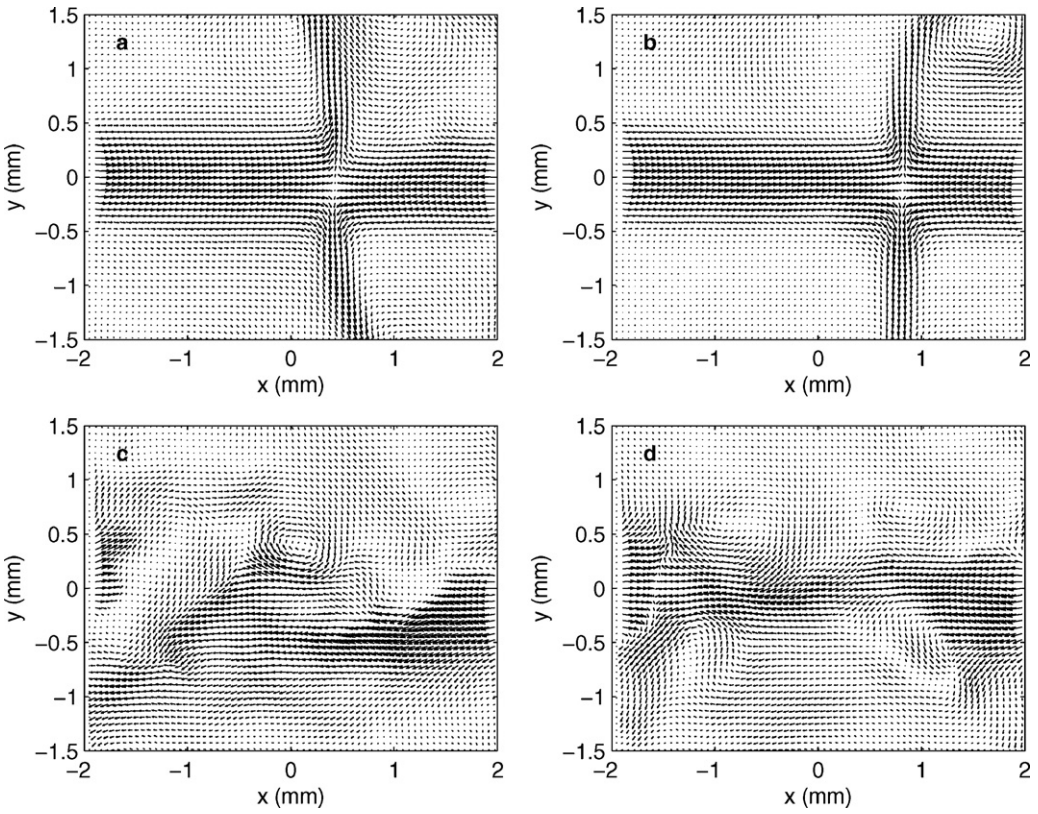

Fig. 3. Four successive instantaneous vector fields obtained with microPIV for $Re = 310$.

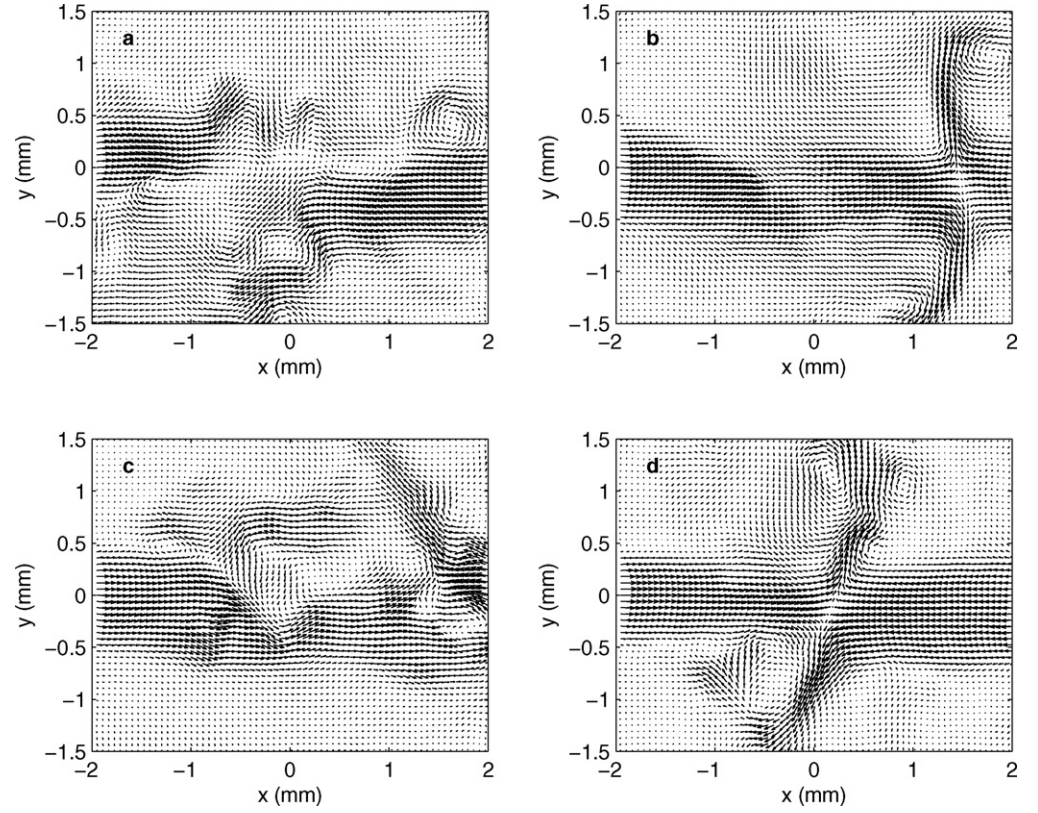

Fig. 4. Four successive instantaneous vector fields obtained with microPIV for $Re = 600$.

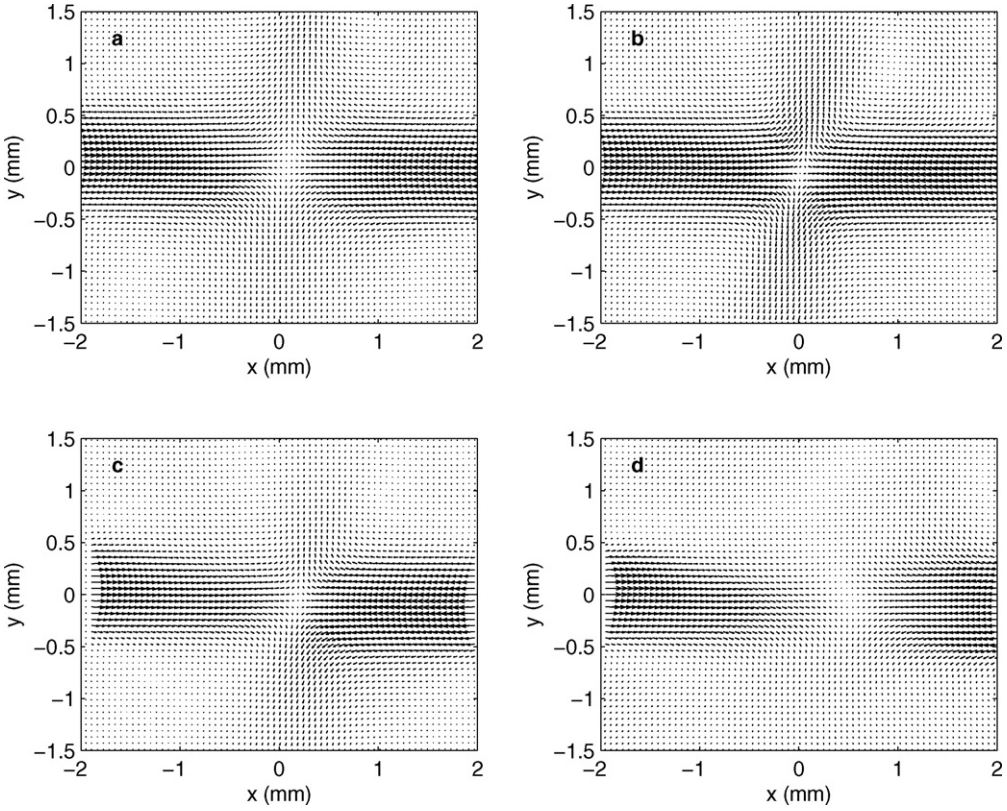

Fig. 5. Mean velocity fields measured by microPIV for (a) $Re = 62$, (b) $Re = 150$, (c) $Re = 310$, (d) $Re = 600$.

mean-square, RMS, of velocity fluctuations, U'^{RMS}) is presented. In particular x-velocity (U_x) and y-velocity (U_y) statistics are represented respectively along the x- and y-axis. Finally a more detailed analysis of the turbulence inside the reactor is carried out with spatial correlations and time spectra of velocity fluctuations. Spatial correlations are normalised as follows [36]:

$$R_{ij}(\mathbf{r}) = \frac{\langle U_i'(\mathbf{x}) U_j'(\mathbf{x}+\mathbf{r})\rangle}{\sqrt{\langle U'^2_i(\mathbf{x})\rangle \langle U'^2_j(\mathbf{x})\rangle}} = \frac{\langle U_i'(\mathbf{x}) U_j'(\mathbf{x}+\mathbf{r})\rangle}{U'^{RMS}_i(\mathbf{x}) U'^{RMS}_j(\mathbf{x})}. \quad (9)$$

where the brackets represent the averaging operator, i and j represent the indexes of two spatial coordinates, $\mathbf{x} = (x, y)$ are the coordinates of the basis point and $\mathbf{r} = (r_x, r_y)$ are the coordinates of the displacements from the basis point. The stagnation point was chosen as base point. While in the simulations it coincides with the centre of the reactor and the axis origin, in the experiments it is slightly off the centre in the positive x-direction. Spatial correlations will be discussed here only for the highest flow rate investigated (i.e., $Re = 600$).

5.1. Experimental instantaneous flow field

The time evolution of the flow field in the CIJR at the different jets Reynolds numbers investigated is here described in terms of the experimental instantaneous velocity vector fields. For brevity only snapshots for $Re = 310$ and 600 are here reported, as the chaotic and turbulent behaviour of the flow field in these conditions is of higher interest for the present study.

For the lowest Reynolds numbers ($Re = 62$) in fact, the instantaneous flow field is almost stationary, except in the centre of the chamber where a continuous but relatively slow motion of the impingement plane is detected without the creation of complicated sub-structures. In these cases, the flow field is well represented by the mean velocity discussed in the next section (see Fig. 5). For $Re = 62$ the instantaneous vector fields show that the flow regime is laminar but unsteady, since the stable impingement plane oscillates from one side to the other of the chamber. At $Re = 150$ the flow regime is still laminar, however its unsteadiness is more pronounced, because of the higher momentum belonging to the jets that causes stronger interactions between the fluid and the walls. Large eddies that interact with the incoming jet streams are created, occasionally causing the temporary disappearance of the impinging plane.

The flow begins to have a chaotic behaviour at $Re = 310$. Four successive snapshots for this case are shown in Fig. 3. The impingement plane shifts more often and more extensively and is periodically broken in many smaller eddies. Finally, as clearly evident in the four consecutive snapshots of the vector field represented in Fig. 4 for $Re = 600$, the flow is fully chaotic, the impingement plane is rarely imaged in the chamber centre, whereas in most images it is replaced by many small eddies that interact with the incoming jets streams, promoting mixing of the two feed streams. The frames reported are not correlated in time, as the 0.25 s interval between successive microPIV vector fields is far to capture the unsteady behaviour of the impingement zone. Their purpose is to qualitatively show the main features of the flow at increasing flow rates. For quantitative comparisons, in the next sections numerical data have been used.

5.2. Mean velocity field

In Fig. 5 the mean flow field measured by microPIV is shown for the four jet Reynolds numbers considered. For all these four conditions the jets entering from the sides of the window are clearly visible. They collide in the centre of the chamber, where the x-momentum becomes null and the flow is deviated radially in the y- and z-directions (as already said the z-direction is not visible because the microPIV images are purely two-dimensional). The

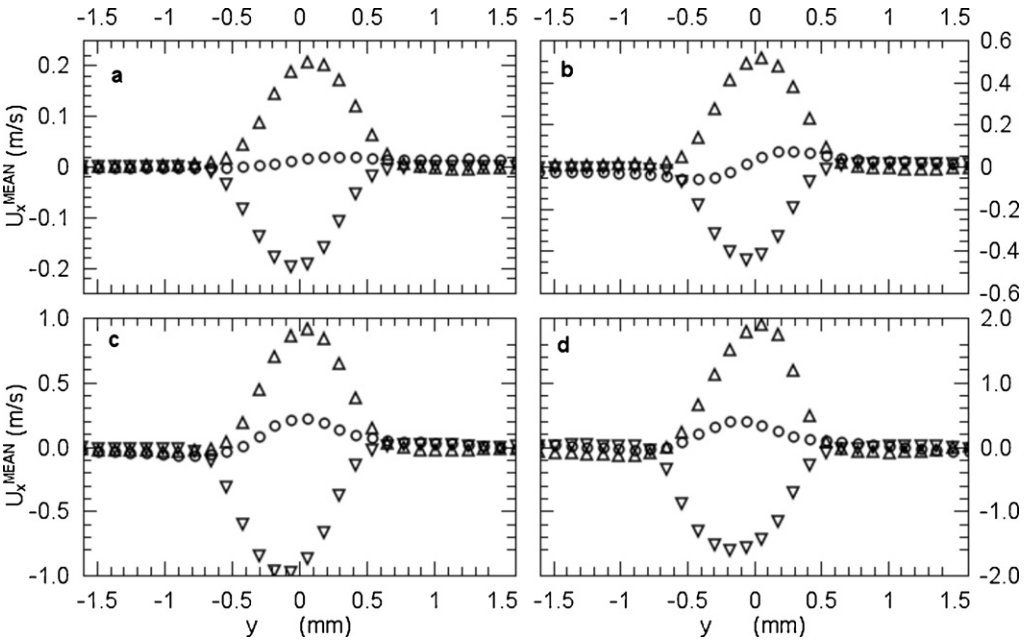

Fig. 6. Profiles of the x-component of the mean velocity measured by microPIV at $x = 0$ mm (○), −2 mm (△), 2 mm (▽) for (a) $Re = 62$, (b) $Re = 150$, (c) $Re = 310$, (d) $Re = 600$.

point of collision of the jets is slightly off the centre for $Re = 600$, because of the great difficulty in exactly balancing the jets with the gear pumps. Unfortunately this difficulty increases as the unsteadiness and turbulence of the flow field increases. This asymmetry between the jets was also taken into account in some of the simulations by a very small difference in the mean velocity of the two jets. However in all cases, it was verified that this unbalance was smaller than 5%.

The profiles of the x-component of the mean velocity (U_x^{MEAN}) measured by means of microPIV are shown in Fig. 6 on three different x-planes, for $x = -2$, 2 and 0 mm and for the four Re considered. The analysis of these data is very important because it allows the assessment of the overall accuracy of the microPIV approach. For the three lowest Re the x-component velocities at $x = \pm 2$ mm are almost identical with a mismatch smaller than about 0.08–0.05 m/s, resulting in velocities for $x = 0$ close to zero. For $Re = 600$ instead the difference between the jets is slightly bigger causing the misalignment of the collision point.

Let us now focus on the comparison between microPIV experiments and DNS simulations. In Fig. 7 the mean velocity in the x-direction (U_x^{MEAN}) along the jets axis normalised with respect to the maximum velocity is reported. The open symbols refer to the experimental data, the continuous line to the DNS with constant inflows (see Eq. (7)) and the dashed line to the DNS predictions with the unsteady boundary conditions (see Eq. (8)). The amplitude of the oscillations K is taken here equal to 1/10, namely the value that

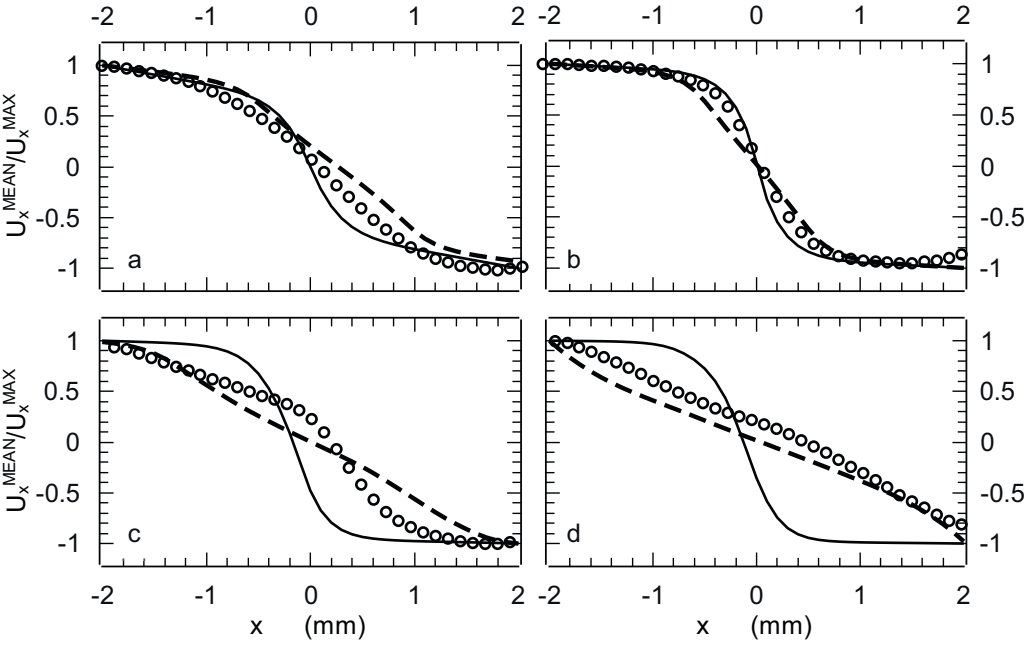

Fig. 7. Comparison between profiles of the x-component of the mean velocity at $y = 0$ mm measured by microPIV (○) and predicted by DNS with constant inflows (continuous line) and DNS with variable inflows (dashed line) for (a) $Re = 62$, (b) $Re = 150$, (c) $Re = 310$, (d) $Re = 600$.

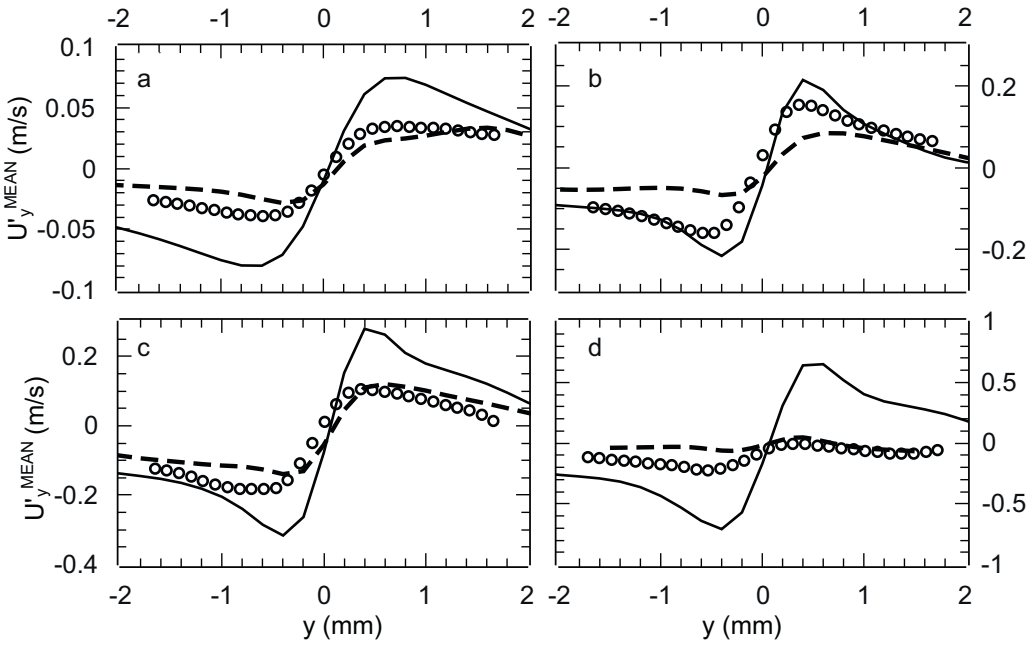

Fig. 8. Comparison between profiles of the y-component of the mean velocity at $x = 0$ mm measured by microPIV (○) and predicted by DNS with constant inflows (continuous line) and DNS with variable inflows (dashed line) for (a) $Re = 62$, (b) $Re = 150$, (c) $Re = 310$, (d) $Re = 600$.

best approximates the experimental inlet. The data are reported for the x-coordinate ranging from −2 mm to 2 mm, covering therefore almost the entire chamber diameter. As it is possible to see, the left and right boundaries of the plot represent the inlet jets that enter the reactor with opposite velocities and then collide in the middle. The comparison between DNS and experiments highlights that the use of unsteady inlet velocities is very important to predict experimental results, as the structure of the impingement is completely changed especially at high flow rates.

These results are particularly interesting when compared with the work of Gavi et al. [37], where a subset of these data were used to validate RANS predictions. In that case constant and laminar inflows were adopted, resulting in satisfactory agreement, proving once again that the importance of accurate unsteady boundary conditions applies mainly to DNS. The same conclusions can be drawn also from the comparison of the mean velocities in the y-direction (U_y^{MEAN}) along the chamber axis, reported in Fig. 8. Also for these quantities, the unsteady inflows strongly influence the predictions resulting in a good agreement with experimental data. The analysis of these two velocity components in other areas of the reactor confirms these conclusions and support our hypothesis that the small instabilities related to the two inlets have a strong influence on the final flow field.

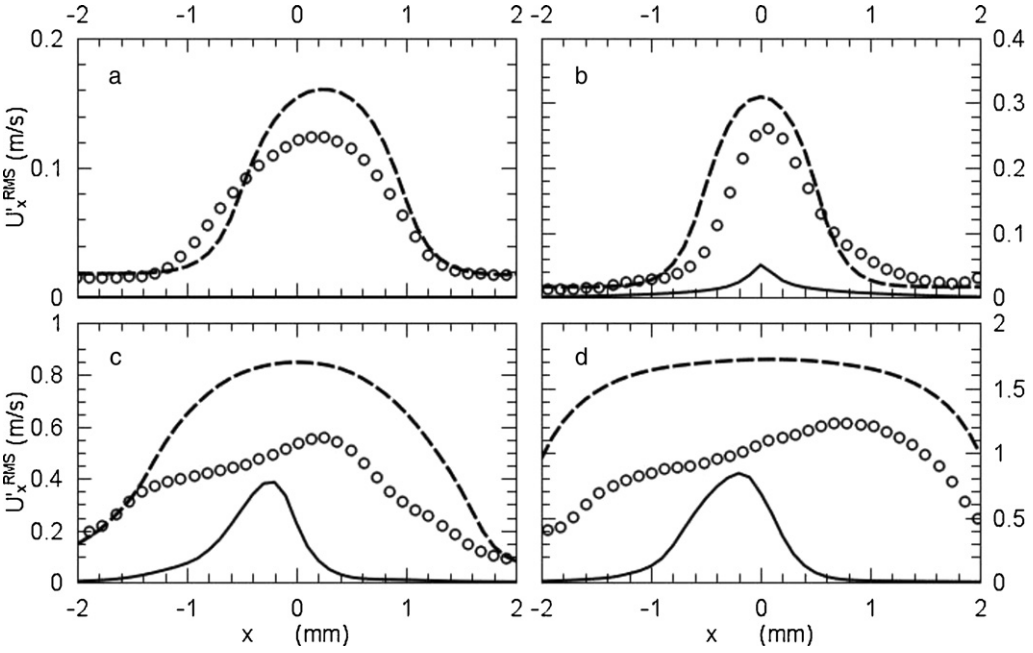

Fig. 9. Comparison between RMS profiles of the x-component of the fluctuating velocity at $y = 0$ mm measured by microPIV (○) and predicted by DNS with constant inflows (continuous line) and DNS with variable inflows (dashed line) for (a) $Re = 62$, (b) $Re = 150$, (c) $Re = 310$, (d) $Re = 600$.

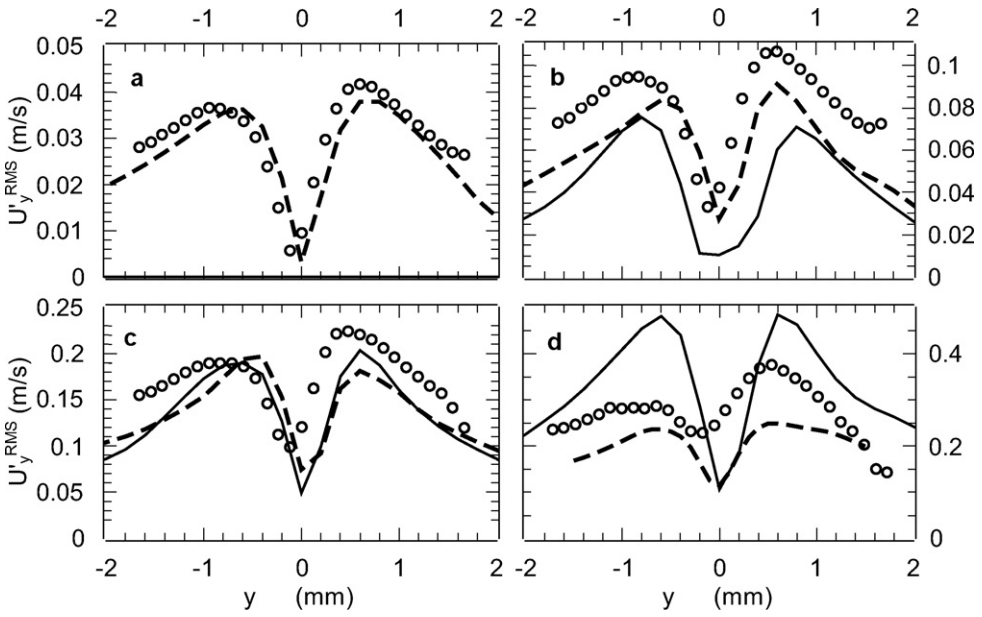

Fig. 10. Comparison between RMS profiles of the *y*-component of the fluctuating velocity at $x = 0$ mm measured by microPIV (◯) and predicted by DNS with constant inflows (continuous line) and DNS with variable inflows (dashed line) for (a) $Re = 62$, (b) $Re = 150$, (c) $Re = 310$, (d) $Re = 600$.

5.3. Velocity fluctuations

As a first example of second order statistics, RMS of velocity fluctuations in the *x*-direction (U'^{RMS}_x) along the jet axis are presented in Fig. 9. Also in this case microPIV experiments (symbols) are compared with DNS predictions with constant (continuous line) and unsteady inflows (dashed line). As it can be observed, with unsteady inflows the velocity fluctuation intensity is predicted reasonably well, while constant inflows strongly underestimate it. In particular, for the lowest flow rates, DNS with steady inflows predicts a steady laminar flow field without fluctuations in disagreement with the experiments. Also looking at the longitudinal fluctuations along the chamber axis reported in Fig. 10, the same consideration holds.

As a general comment it is possible to state that, especially for high flow rates, the oscillations are slightly over-predicted. This can be due to different reasons. As already reported different spatial resolutions were used in microPIV experiments and simulations. In fact, microPIV has a lower resolution and it may not capture small scales that are instead included in the numerical results. However, when the spatial filter was activated to reproduce the microPIV resolution a small and not relevant improvement was observed. Most likely this small overestimation could be caused by the approximation of the inflow boundary conditions with a single oscillating frequency with the assumption of phase opposition.

5.4. Spatial correlations

Spatial correlations were calculated from experiments and simulations according to Eq. (9) in order to further investigate some specific features of the flow field in the CIJR. However, as previously mentioned, the most interesting results are observed at the highest jets Reynolds number investigated in this work and therefore the results discussed in this section are limited to $Re = 600$. In Fig. 11 R_{xx}, R_{yy} and R_{xy} are shown both for microPIV experiments (left) and DNS (right). R_{xx} (top) presents a small area of high correlation around the base point, and the correlation is non-zero and positive in a wide area that contains the jet streams. This shape is confirmed by the results reported in Fig. 5(d). In fact, as can be seen due to the jets presence the *x*-component of velocity changes slowly along the jets axis, causing the correlation R_{xx} to remain high over long distances in the *x*-direction. In microPIV measurements the correlation decrease faster along the jet axis with respect to simulations. This small difference can be explained again with the approximation of inflow conditions with a single frequency and with the different numbers and lengths of time steps. The correlation R_{yy} for both experiments and simulations is a plume centred at the base point above the jets axis, almost symmetric with respect to the chamber axis (and always positive). A second plume of low negative correlation is situated symmetrically to the first, below the jets axis, consistently with what reported in Figs. 5(d) and 4. Along the jet-axis in fact the *y*-component of the velocity is almost zero, whereas along the chamber axis the same component is rather high and changes only a little, determining the high R_{yy} correlation. Finally the correlation R_{xy} is symmetric with respect to an axis inclined 45° to the chamber and jets axes. The correlation is negative in the first and third quadrants, whereas it is positive in the second and fourth quadrants. Again the reason for this can be understood by observing the snapshots reported in Fig. 4. The eddies that are formed by the jet with positive *x*-component velocity rotate anti-clock wise above the jets axis and clock wise below the jets axis, therefore originating a negative *y*-component velocity above and a positive *y*-component velocity below the jets axis. A similar situation can be described for the opposite jet with negative *x*-component velocity.

5.5. Time series power spectra

The important effects of imposing oscillating inflows in the simulations is also visible in Fig. 12 where the power spectra of *x*-velocity fluctuations (from DNS) in the impingement point are reported for $Re = 310$ (dashed line) and $Re = 600$ (continuous line). The spectra are smoothed using a 7-points moving average to remove the noise at high frequencies. As it can be seen, the imposed oscillations are very small in amplitude but they create a wide range of frequencies in the spectrum of velocity fluctuations. The spectra exhibit marked peaks reflecting the oscillations in the inflow (main mode), followed by sub-harmonics, increasing (non-linearly) in frequencies with the Reynolds number. For the two lowest flow rates the peak contains more than 90% of the energy while for $Re = 310$ and $Re = 600$ the percentage decreases to 73% and 55%, respectively. The remaining energy is transferred to smaller scales. Increasing

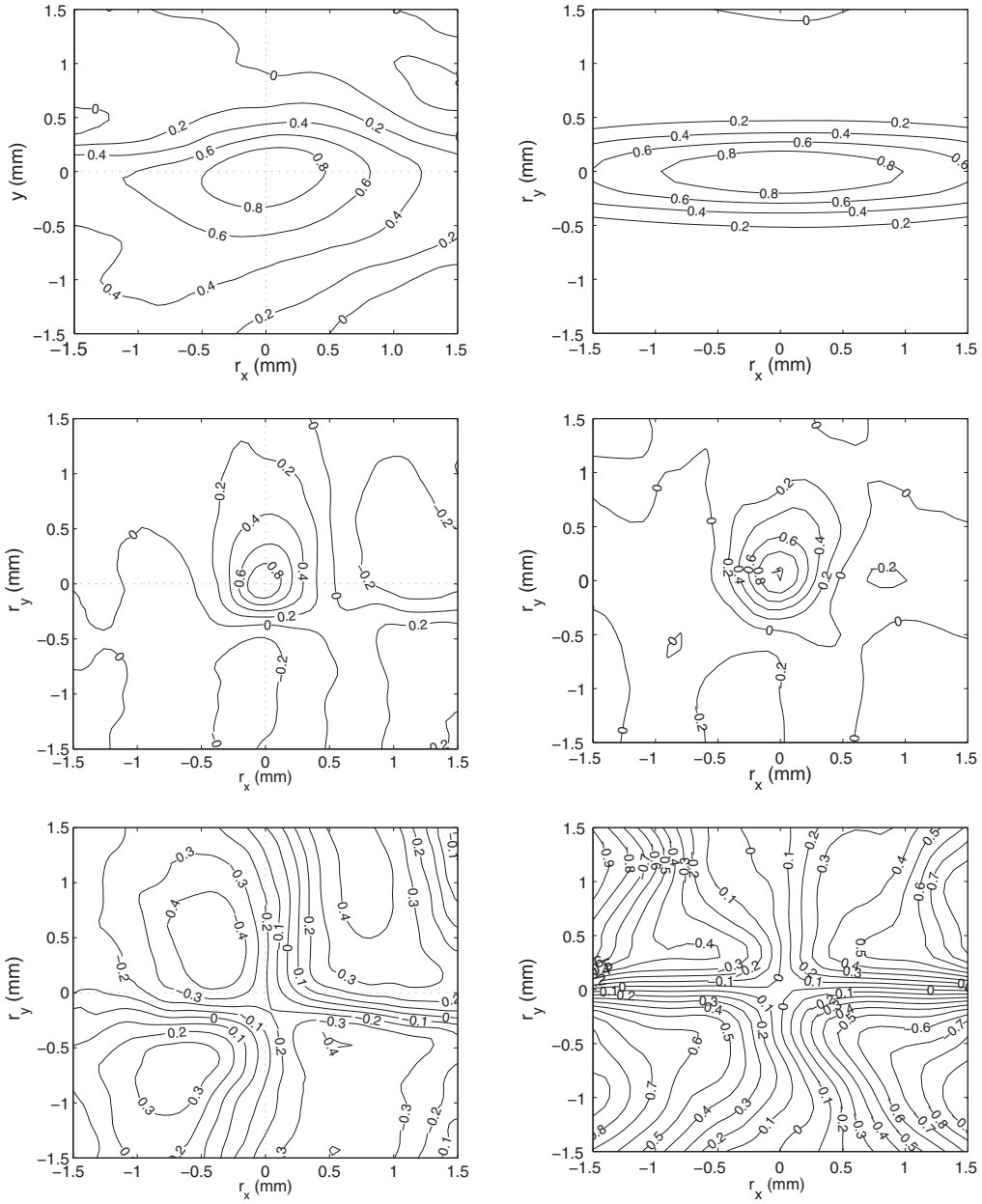

Fig. 11. From top to bottom spatial correlation functions R_{xx}, R_{yy} and R_{xy} as measured by microPIV (left) and simulations (right) for $Re = 600$.

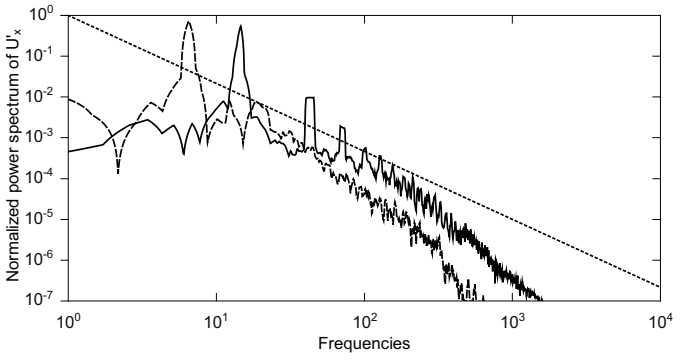

Fig. 12. Normalised power spectra of the time series of x-velocity fluctuations in the impingement point for $Re = 310$ (dashed line) and for $Re = 600$ (continuous line) compared with the characteristic cascade slope for three-dimensional turbulence (dotted straight line).

the flow rate the power spectrum tends to approach the −5/3 logarithmic slope, characteristic of three-dimensional turbulence. This result shows that the flow in the reactor is not fully turbulent but it is in a transitional regime. Furthermore it can be noted that the approximation of the experimental inflows with a single frequency oscillation is reasonable for the purpose of simulating the behaviour of the system. A sensitivity analysis modifying the frequency, the phase displacement between the two inlets and the amplitude of oscillations within a reasonable range revealed a weak influence of these parameters on the qualitative behaviour of the system and on the velocity statistics analysed.

6. Conclusions

In this work the flow field in a CIJR measured with microPIV and predicted via DNS was presented and discussed qualitatively and quantitatively in terms of first and second order statistics at four different flow regime conditions ($Re = 62$, 150, 310 and 600).

Only the combination of the experimental and modelling approach was found to be able to address the many physical issues involved. MicroPIV, here applied for the first time to a three-dimensional axisymmetric CIJR, is able to highlight the presence of a rich variety of flow structures and instabilities. In particular it emerges that the flow field is laminar and unsteady for low jets Reynolds numbers ($Re < 310$), and turbulent for and higher values. However these turbulent features increase the difficulties in the experimental setup and make it extremely hard to understand and fully explain the results. DNS can therefore be used to gain further insights in the system. Our results show that the natural instability generated by the impingement of the jets is not enough to explain the chaotic behaviour of the system. Instead, if more accurate inflow conditions are imposed in DNS, by introducing small oscillations similar to the experimental ones, a more chaotic behaviour is observed. These oscillations are not obtained with a fitting procedure but simply imposed according to the experimental data available in the inlets, which revealed small variations in time due to the feeding system. Since the main purpose of this study is to understand what happens in micro-reactors applied in industries for continuous operation, it is very important to analyse the effects of the unsteadiness acting and generated by the system, and there is no interest in artificially removing these oscillations but they must be taken into account in the computational model. DNS with a proper approximation of the boundary conditions resulted in very good agreement with experimental data and provided us with an explanation of the structures observed with microPIV: the breakup of the impingement plane generates many eddies of different sizes that enhance turbulence in the device and its mixing performance. These results suggest also that unsteady simulations of this type of micro-mixers must be provided with accurate unsteady boundary conditions, and this gave the way for the next step of the work that includes the use of LES with appropriate sub-grid scale models for the simulations of mixing and reactions in CIJR.

Acknowledgements

The research has been partially supported by an Italian National Research Project (PRIN) grant (Multi-scale Modelling and Development of Process Reactors for Polymeric Nano-particle Precipitation). Moreover, the financial support of Ascomp GmbH and of the Italian Ministry of Education, University and Research is gratefully acknowledged. The authors also wish to thank Alessio Zaccone for the suggestion of using urea to correct the refractive index and the staff of Ascomp GmbH for their technical support in the simulations setup.

References

[1] D. Horn, J. Rieger, Organic nanoparticles in the aqueous phase—theory, experiment, and use, Angew. Chem. Int. Ed. 40 (2001) 4330–4361.
[2] O.V. Salata, Applications of nanoparticles in biology and medicine, J. Nanobiotechnol. 2 (2004) 177–182.
[3] B.K. Johnson, R.K. Prud'homme, Flash nanoprecipitation of organic actives and block copolymers using a Confined Impinging Jets Mixer, Aust. J. Chem. 56 (2003) 10–21.
[4] J. Kipp, The role of solid nanoparticle technology in the parenteral delivery of poorly water-soluble drugs, Int. J. Pharm. 284 (2004) 109–122.
[5] F. Lince, D.L. Marchisio, A.A. Barresi, Strategies to control the particle size distribution of poly-ε-caprolactone nanoparticles for pharmaceutical applications, J. Colloid Interface Sci. 322 (2008) 505–515.
[6] J. Gradl, H.C. Schwarzer, F. Schwertfirm, M. Manhart, W. Peukert, Precipitation of nanoparticles in a T-mixer: coupling the particle population dynamics with hydrodynamics through Direct Numerical Simulation, Chem. Eng. Process. 45 (2006) 908–916.
[7] Y. Liu, J.C. Cheng, R.K. Prud'homme, R.O. Fox, Mixing in a multi-inlet vortex mixer (MIVM) for flash nano-precipitation, Chem. Eng. Sci. 63 (2008) 2829–2842.
[8] J.C. Cheng, M.G. Olsen, R.O. Fox, A microscale multi-inlet vortex nanoprecipitation reactor: turbulence measurement and simulation, Appl. Phys. Lett. 94 (2009) 104–204.
[9] E. Gavi, L. Rivautella, D.L. Marchisio, M. Vanni, A.A. Barresi, G. Baldi, CFD Modelling of nano-particle precipitation in confined impinging jet reactors, Chem. Eng. Res. Des. 85 (2007) 735–744.
[10] B.K. Johnson, R.K. Prud'homme, Chemical processing and micromixing in confined impinging jets, AIChE J. 49 (2003) 2264–2282.
[11] Y. Liu, R.O. Fox, CFD predictions for chemical processing in a confined impinging-jets reactor, AIChE J. 52 (2006) 731–744.
[12] D.L. Marchisio, R.O. Fox, Solution of population balance equations using the direct quadrature method of moments, J. Aerosol Sci. 36 (2005) 43–73.
[13] E. Gavi, D.L. Marchisio, A.A. Barresi, CFD modelling and scale-up of Confined Impinging Jet Reactors, Chem. Eng. Sci. 62 (2007) 2228–2241.
[14] J.G. Santiago, S.T. Wereley, C.D. Meinhart, D.J. Beebe, R.J. Adrian, A particle image velocimetry system for microfluidics, Exp. Fluids 25 (1998) 316–319.
[15] H. Li, R. Ewoldt, M.G. Olsen, Turbulent and transitional velocity measurements in a rectangular microchannel using microscopic particle image velocimetry, Exp. Therm. Fluid Sci. 29 (2005) 435–446.
[16] V. Van Steijn, T.M. Kreutzer, C.R. Kleijn, MicroPIV study of the formation of segmented flow in microfluidic T-junctions, Chem. Eng. Sci. 62 (2007) 7505–7514.
[17] Y. Liu, M.G. Olsen, R.O. Fox, Turbulence in a microscale planar confined impinging-jets reactor, Lab Chip 9 (2009) 1110–1118.
[18] C.C. Landreth, R.J. Adrian, Impingement of a low Reynolds number turbulent circular jet onto a flat plate at normal incidence, Exp. Fluids 9 (1990) 74–84.
[19] F. Schwertfirm, J. Gradl, H.C. Schwarzer, W. Peukert, M. Manhart, The low Reynolds number turbulent flow and mixing in a confined impinging jet reactor, Int. J. Heat Fluid Flow 28 (2007) 1429–1442.
[20] R.J. Santos, E. Erkoç, M.M. Dias, A.M. Teixeira, J. Carlos, Hydrodynamics of the mixing chamber in RIM: PIV flow-field characterization, AIChE J. 54 (2008) 1153–1163.
[21] H. Feng, M.G. Olsen, Y. Liu, R.O. Fox, J.C. Hill, Investigation of turbulent mixing in a confined planar-jet reactor, AIChE J. 51 (2005) 2649–2664.
[22] S.T. Wereley, L. Gui, C.D. Meinhart, Advanced algorithms for microscale particle image velocimetry, AIAA J. 40 (2002) 1047–1055.
[23] A.K. Prasad, Particle image velocimetry, Curr. Sci. 79 (2000) 51–60.
[24] K. Kawahara, C. Tanford, Viscosity and density of aqueous solutions of urea and guanidine hydrochloride, J. Biol. Chem. 241 (1966) 3228–3232.
[25] J.R. Warren, J.A. Gordon, On the refractive indices of aqueous solutions of urea, J. Phys. Chem. 70 (1966) 297–300.
[26] M. Samimy, S.K. Lele, Motion of particles with inertia in a compressible free shear layer, Phys. Fluids A 3 (1991) 1915–1923.
[27] M.G. Olsen, R.J. Adrian, Out-of-focus effects on particle image visibility and correlation in microscopic particle image velocimetry, Exp. Fluids 29 (2000) S166–S174.
[28] M.G. Olsen, R.J. Adrian, Brownian motion and correlation in particle image velocimetry, Opt. Laser Technol. 32 (2000) 621–627.
[29] M.G. Olsen, C.J. Bourdon, Out-of-plane motion effects in microscopic particle image velocimetry, J. Fluids Eng. 125 (2003) 895–901.
[30] M.G. Olsen, Directional dependence of depth of correlation due to in-plane fluid shear in microscopic particle image velocimetry, Meas. Sci. Technol. 20 (2009) 015402.
[31] Ascomp GmbH, Multi-Fluid Navier–Stokes Solver TransAT User Manual, 2009.
[32] J. Zhu, A low-diffusive and oscillation-free convection scheme, Commun. Appl. Numer. Methods 7 (1991) 225–232.
[33] J.H. Ferziger, M. Peric, Computational Methods for Fluid Dynamics, third edition, Springer-Verlag, Berlin, 2002.
[34] S.M. Hosseinalipour, A.S. Mujumdar, Comparative evaluation of different turbulence models for confined impinging and opposing jet flows, Numer. Heat Transfer Part A 28 (1995) 647–666.
[35] K. Abe, T. Kondoh, Y. Nagano, A new turbulence model for predicting fluid flow and heat transfer in separating and reattaching flows: I. Flow field calculations, Int. J. Heat Mass Transfer 37 (1994) 139–151.
[36] M.G. Olsen, J.C. Dutton, Stochastic estimation of large structures in an incompressible mixing layer, AIAA J. 40 (2002) 2431–2438.
[37] E. Gavi, D.L. Marchisio, A.A. Barresi, M.G. Olsen, R.O. Fox, Turbulent precipitation in micromixers: CFD simulation and flow field validation, Chem. Eng. Res. Des. 88 (2010) 1182–1193.